Journal of Advanced Ceramics
2021, **10**(5): 1119–1128
https://doi.org/10.1007/s40145-021-0497-7

ISSN 2226-4108
CN 10-1154/TQ

Research Article

Photocurrent density and electrical properties of $Bi_{0.5}Na_{0.5}TiO_3$–$BaNi_{0.5}Nb_{0.5}O_3$ ceramics

Mingqiang ZHONG[a,b], Qin FENG[c], Changlai YUAN[a,b,*], Xiao LIU[a,b], Baohua ZHU[b], Liufang MENG[b], Changrong ZHOU[a,b], Jiwen XU[a,b], Jiang WANG[a,b,*], Guanghui RAO[a,b,d,*]

[a]*Guangxi Key Laboratory of Information Materials*, *Guilin University of Electronic Technology*, *Guilin 541004*, *China*
[b]*College of Material Science and Engineering*, *Guilin University of Electronic Technology*, *Guilin 541004*, *China*
[c]*School of Resources*, *Environment and Materials*, *Guangxi University*, *Nanning 530004*, *China*
[d]*Institute of Physics*, *Chinese Academy of Sciences*, *Beijing 100190*, *China*

Received: January 25, 2021; Revised: May 9, 2021; Accepted: May 10, 2021

Abstract: In this work, the $(1–x)Bi_{0.5}Na_{0.5}TiO_3–xBaNi_{0.5}Nb_{0.5}O_3$ (BNT–BNN; $0.00 \leqslant x \leqslant 0.20$) ceramics were prepared via a high-temperature solid-state method. The crystalline structures, photovoltaic effect, and electrical properties of the ceramics were investigated. According to X-ray diffraction, the system shows a single perovskite structure. The samples show the normal ferroelectric loops. With the increase of BNN content, the remnant polarization (P_r) and coercive field (E_c) decrease gradually. The optical band gap of the samples narrows from 3.10 to 2.27 eV. The conductive species of grains and grain boundaries in the ceramics are ascribed to the double ionized oxygen vacancies. The open-circuit voltage (V_{oc}) of ~15.7 V and short-circuit current (J_{sc}) of ~1450 nA/cm^2 are obtained in the 0.95BNT–0.05BNN ceramic under 1 sun illumination (AM1.5G, 100 mW/cm^2). A larger V_{oc} of 23 V and a higher J_{sc} of 5500 nA/cm^2 are achieved at the poling field of 60 kV/cm under the same light conditions. The study shows this system has great application prospects in the photovoltaic field.

Keywords: $Bi_{0.5}Na_{0.5}TiO_3$–$BaNi_{0.5}Nb_{0.5}O_3$; ferroelectric semiconductors; optical band gap; photovoltaic effect; impedance spectroscopy

1 Introduction

Growing energy shortage and deterioration of the environment promote the research and utilization of new energy. Photovoltaic technology and industry have been developed rapidly under the condition of current energy crisis [1–4]. Solar cells based on traditional silicon-based technology are widely used in reality, but the high price of raw materials limits its further development [5]. Fortunately, the ferroelectric photovoltaic (FEPV) effect observed in perovskite materials has aroused great interest of researchers because of its potential in solar cells with good stability

* Corresponding authors.
E-mail: C. Yuan, yclai-2002@163.com, yuanchanglai@guet.edu.cn;
J. Wang, waj124@guet.edu.cn;
G. Rao, rgh@guet.edu.cn

and easily available raw materials [6–9]. Much work has been done about the FEPV effect in ferroelectric perovskite oxides, such as $BiFeO_3$ [10,11], $BaTiO_3$ [12–15], and $Bi_{0.5}Na_{0.5}TiO_3$ (BNT) compounds [16]. Unfortunately, the bandgaps of most perovskite-oxide ferroelectrics are higher than 3.2 eV. For energy utilization, ferroelectric materials absorbing ultraviolet (UV) rays containing only 3.5% of solar radiation intensity are of little significance [17]. Therefore, an adjustable narrow-band gap is of great significance for improving the photovoltaic effect of ferroelectric materials.

As one of the classic perovskite-oxide ferroelectrics, $Bi_{0.5}Na_{0.5}TiO_3$ (BNT) has attracted considerable attention in the photovoltaic field due to its large spontaneous ferroelectric polarization, high large opto-electrical coefficient, and adjustable band gap [18]. A lot of research have been done by the researchers on the outstanding properties of dielectric [19], piezoelectric [20], and ferroelectric of BNT materials [21]. Unfortunately, there are few of research on the photovoltaic applications based on BNT materials. As an environmentally friendly ferroelectric material, BNT exhibits a high Curie temperature (T_C) of ~320 ℃ and large residual polarization (P_r) of ~38 μC/cm^2 [22]. The large spontaneous polarization of BNT can make it possible for their photovoltaic applications, due to that the light-excited carriers can be effectively separated under the internal bias field formed by spontaneous polarization of ferroelectrics [23–25]. However, the bandgaps of pure BNT is higher than 3.1 eV, and thus the absorption of light is mainly in the deep UV region, which restricts their development in the field of photovoltaics [26].

In recent years, much effort had been done by researchers to optimize the optical characteristics of BNT materials. For example, $Bi_{0.5}Na_{0.5}TiO_3$–$NiTiO_3$ [27], $Bi_{0.5}Na_{0.5}TiO_3$–$SrFeO_{3-\delta}$ [28], $Bi_{0.5}Na_{0.5}TiO_3$–$SrMnO_{3-\delta}$ [29], and $Bi_{0.5}Na_{0.5}TiO_3$–$MgCoO_{3-\delta}$ [30] were successfully prepared by Dang Duc Dung and co-workers. The band gap and ferroelectric properties of BNT can be regulated by substitution at the A/B sites of perovskite oxides. For example, Grinberg *et al.* [23] first described that the introduction of $BaNi_{0.5}Nb_{0.5}O_3$ could reduce the band gap of pure $KNbO_3$ and produce a higher J_{sc} of 100 nA/cm^2.

Based on the above considerations, the $BaNi_{0.5}Nb_{0.5}O_3$-doped $Bi_{0.5}Na_{0.5}TiO_3$ materials were chosen as the research object. In this work, the influence factors (polarization, light intensity) of photocurrent density were studied systematically. Under one sun AM1.5G illumination (100 mW/cm^2) and after the polarization, a J_{sc} of ~5500 nA/cm^2 for the sample with x = 0.05 is achieved, which is about 55 times larger than that of KBNNO ceramic [23]. Furthermore, the crystal structures and electrical properties of the system were also characterized in detail.

2 Experimental details

The $(1–x)Bi_{0.5}Na_{0.5}TiO_3$–$xBaNi_{0.5}Nb_{0.5}O_3$ (BNT–BNN; $0.00 \leqslant x \leqslant 0.20$) lead-free ceramic samples were synthesized by a solid-state reaction technique. The Na_2CO_3 (> 99%, Aladdin, China), $BaCO_3$ (> 99.5%, Aladdin, China), NiO (> 98%, Aladdin, China) (> 99.5%, Aladdin, China), Nb_2O_5 (> 99.9%, Aladdin, China), Bi_2O_3 (> 99%, Aladdin, China), and TiO_2 (> 99%, Aladdin, China) were used as raw materials and milled in anhydrous ethanol medium for 24 h. After that, these mixed powders were dried, sieved, and calcined at 900 ℃ for 12 h. Subsequently, the powders were pressed into pellets with 5 wt% polyvinyl alcohol (PVA) binder under 100 MPa. At last, the pellets were heated at 600 ℃ for 2 h to burn out the PVA binder and calcined at the temperature range 1100–1140 ℃ for 3 h.

The crystalline structure was determined via X-ray diffraction (XRD, PLXCEL 3D, PANALYTICAL, the Netherlands), ranging from 20° to 80°. The surface morphology was observed with scanning electron microscope (FE-SEM, Quanta FEG-450, FEI, USA). Transmission electron microscopy (TEM) images were observed using FEI talosf200s microscopes operating at an accelerating voltage of 200 kV. The lattice vibration modes of the ceramics were recorded by Raman spectra (Horiba Jobin-Yvon Inc., Paris, France). The electric induced polarization loops (P–E) were recorded via a ferroelectric (FE) test equipment (TF Analyzer 2000HS, AACHEN, Germany). The light absorption efficiency of the samples was measured via a UV–Vis–NIR (Lambda 750 s) spectrophotometer. The impedance analyzer (Agilent 4294A, USA) helped to measure the impedance spectroscopy in frequencies (40–10^6 Hz) and at temperatures (400–650 ℃). In order to test the photovoltaic effect of the sample, a layer of indium tin oxide (ITO) film electrode was sputtered on one side of the ceramic samples and silver was pasted on the other surface. The composite ceramic device has the diameter of 10 mm and thickness of

0.30 mm. The *J–V* curves of samples under simulated illumination were measured by 2410 light source instrument.

3 Results and discussion

The XRD spectra of (1–*x*)BNT–*x*BNN ceramic samples are shown in Fig. 1. These patterns illustrate a pure perovskite structure phase without any trace of secondary phases. The pure BNT ceramic samples are indexed well to the standard JCPDS Card No. 04-011-0431. With the addition of BNN, the (104) and (110) peaks gradually merge, reflecting a change of its structure (rhombohedral to tetragonal structures). A magnification within the 2θ range of 31° to 34° is shown in Fig. 1(b). As the BNN fraction in the solid solutions increases, the (104)/(110) peaks shifted towards lower 2θ angles, ascribed to the increase in lattice parameters and cell volume as a function of the BNN fraction [31–33].

The SEM analyses were performed for the (1–*x*)$Bi_{0.5}Na_{0.5}TiO_3$–*x*$BaNi_{0.5}Nb_{0.5}O_3$ (BNT–BNN; 0.00 ⩽ *x* ⩽ 0.20) ceramic morphology in Fig. 2. Figure 2 illustrates a typical 3000× SEM micrograph of sample ceramics with highly dense and free-void grains. It can be seen from the figure that *x* = 0.05 has a denser morphology and the smallest grain size. Generally, the photovoltaic effect in ferroelectric materials correlates with the grain size effect [5]. The full density and homogenous microstructures with small grain size are the important factor on the improvement of photocurrent. It is believed that the smaller grain size of the samples will form more defects in grain boundary, which can provide more absorbing centers inside the samples. The carriers will be trapped inside the samples, which

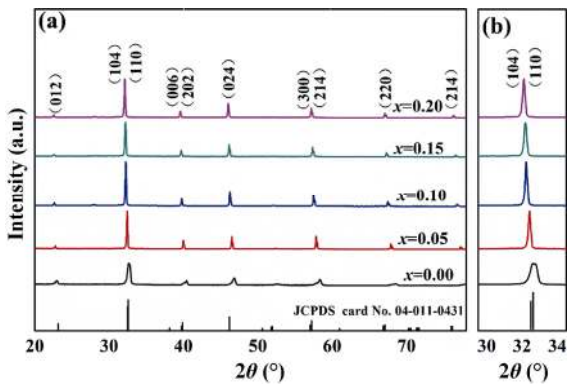

Fig. 1 (a) XRD patterns of pure and $BaNi_{0.5}Nb_{0.5}O_3$-modified $Bi_{0.5}Na_{0.5}TiO_3$ ceramics; (b) locally magnified patterns at 2θ = 30°–34°.

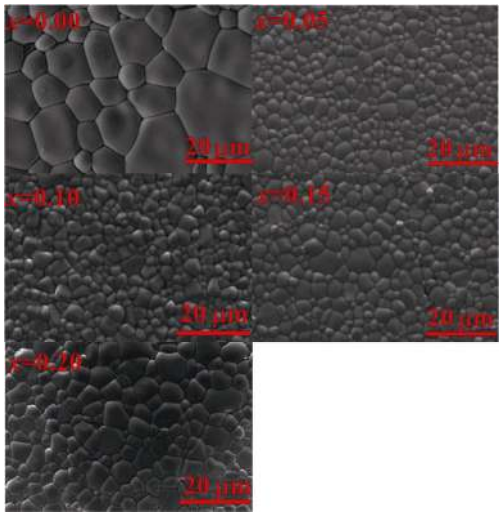

Fig. 2 SEM images of the (1–*x*)$Bi_{0.5}Na_{0.5}TiO_3$–*x*$BaNi_{0.5}Nb_{0.5}O_3$ (BNT–BNN; 0.00 ⩽ *x* ⩽ 0.20).

will form an electro-potential barrier and lead to the larger photocurrent [34].

The Raman diffraction is an advantageous mean of characterization, which can provide accurate information about the local deformation and ion configuration in the crystal structure. At ambient temperature, Fig. 3(a) represents the Raman scattering spectra of (1–*x*)BNT–*x*BNN (*x* = 0.00–0.20) ceramic samples in a wave number from 100 to 1000 cm^{-1}. About four regions were detected in the spectra, and they are nearly identical to those previously reported for BNT-based ceramics [35]. Figure 3(b) exhibits the Raman spectroscopy of the *x* = 0.05 ceramic sample fitted by Gaussian peak functions. The measured region (100–1000 cm^{-1}) of the ceramic samples can be deconvoluted into six main peaks, which are located at 116, 273, 524, 600, 727, and 790 cm^{-1}. The peak at 116 cm^{-1} is mainly affected by the Na–O bonds of the A-site vibration in the ABO_3 style perovskite ceramics [36]. The peak at 274 cm^{-1} is only related to the bending motion of O–Ti–O, which is also very susceptible to phase transformation [37,38]. The Raman peak in the range of 400–700 cm^{-1} is mainly attributed to the stretching symmetric vibration mode of TiO_6 octahedron [39]. After 700 cm^{-1}, the Raman peak is mainly related to the two longitudinal optical overlapped peaks, A1 (longitudinal optical) and E (longitudinal optical) [40]. The XRD patterns and Raman analysis indicate that the $BaNi_{0.5}Nb_{0.5}O_3$ can be incorporated into the $Bi_{0.5}Na_{0.5}TiO_3$ matrix to form a new solid solution.

Figure 4 illustrates the polarization loops of (1–*x*)BNT–*x*BNN ceramic samples with *x* = 0.00–0.20.

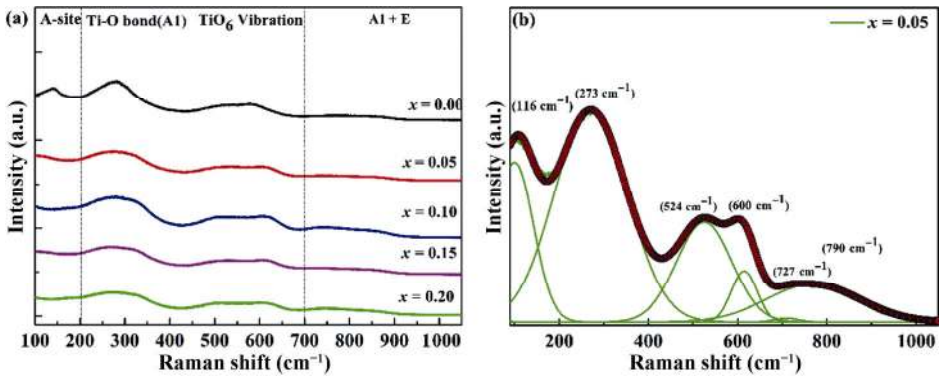

Fig. 3 (a) Raman scattering spectra of the ceramic samples; (b) Raman deconvolution of x = 0.05 sample.

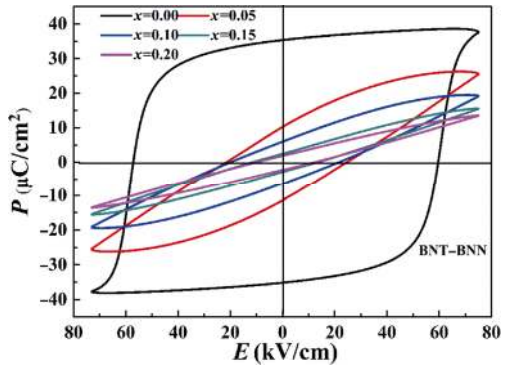

Fig. 4 Electric induced polarization loops (P–E) of (1–x)BNT–xBNN (x = 0–0.20) ceramic samples.

All the ceramics show typical ferroelectric hysteresis loops. With the increasing x, the maximum residual polarization value (P_r) and the coercive field (E_c) of the ceramics decrease gradually. The decrease of P_r can mainly be due to the phase transition from ferroelectric to paraelectric [41]. Oxygen vacancy led to this phenomenon. The substitution of Ti^{5+} by Ni^{2+} results in the long-range ordered displacement of Ti^{5+} and structural local strain. Considering the electronegativity of Ba and Na, the ionic strength of the modified A–O bond is partially replaced with Ba^{2+} at the A-site. Furthermore, with the change of the grain size of the ceramic samples, the grain boundary and defects will have pinning effect on the domain and lead to the decrease of E_c [42].

Figures 5(a)–5(e) illustrate the change of the dielectric constant (ε_r) and dielectric loss (tanδ) of the ceramic samples in different frequency ranges with temperature. It can be observed that with the increase of temperature, ε_r increases gradually, reaches the maximum value at Curie temperature (T_C), and then

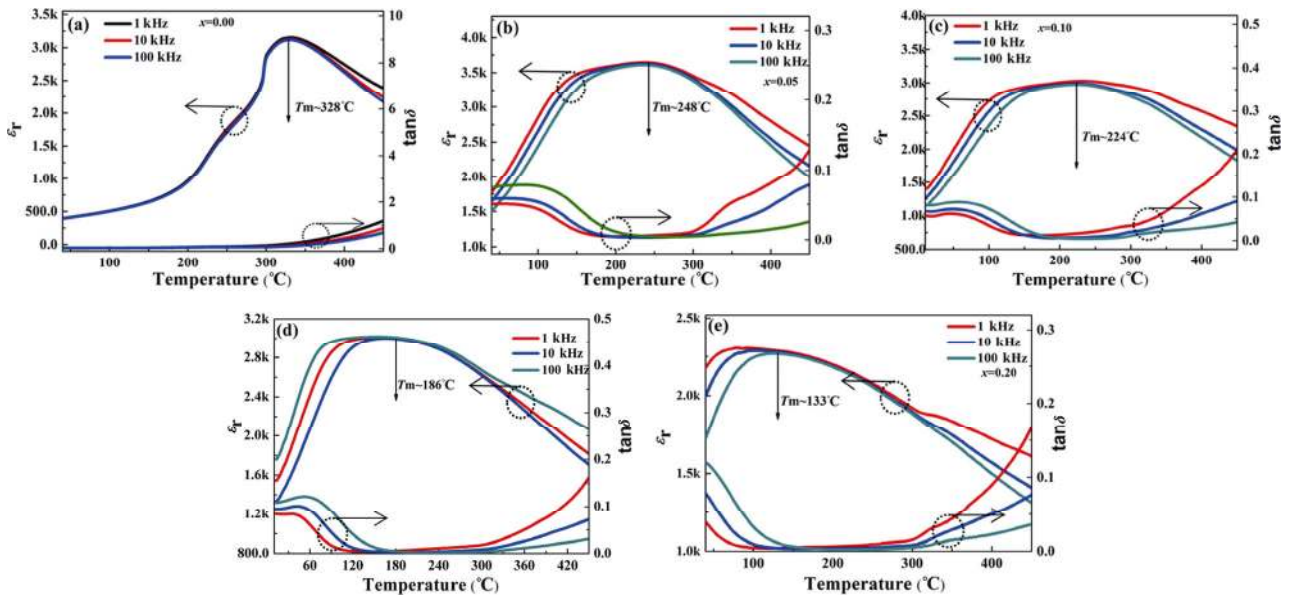

Fig. 5 Relative permittivity and tanδ versus temperatures for the ceramic samples: (a) pure BNT, (b) 0.95BNT–0.05BNN, (c) 0.90BNT–0.10BNN, (d) 0.85BNT–0.15BNN, (e) 0.80BNT–0.20BNN.

decreases gradually. At the same time, before the T_C, the relative permittivity of low-frequency gradually increases with the increase of the test temperature, which may be related to the polarization and conductivity of space charges in the samples [43]. The tanδ increases sharply above ~T_C. It could be due to the loss of some bismuth and sodium oxide during the sintering process, as well as the resulting defect chemical changes, resulting in ionic and electronic conduction inside the samples, which causes the rise in tanδ [44,45].

Complex impedance spectroscopy (CIS) is an effective method to detect the electrical properties of conductive interface for ceramics. At the same time, it can also be used to analyze moving charge carriers and bond dynamics in solid or liquid mixtures (insulating layer, semiconductor, ion). Moreover, the physical process inside the sample can be identified by the corresponding equivalent circuit model [46]. Figures 6(a) and 6(b) illustrate the Cole–Cole plots of 0.95BNT–0.05BNN ceramics from 400 to 650 ℃. The Cole–Cole plots can be fitted by two parallel R–CPE–C elements connected in series in inset of Fig. 6(a). It can be observed that the radius of the arcs gradually decreases with increasing temperature, indicating the resistance of 0.95BNT–0.05BNN ceramic decreases with the increase of the test temperature. The result can also reflect these ceramic samples have the negative temperature coefficient of resistance (NTCR) effect. In order to evaluate the rationality of the equivalent circuit and the accuracy of fitting data, we calculated the impedance residuals of Z' and Z'', which reflect the difference between experimental and fitting data, as show in Fig. 6(c). Residual values of Z' and Z'' are in the range of (−0.0001)–(+0.0003), suggesting that the fitting data are reliable. Figure 6(d) illustrates the Arrhenius-type plots of 0.95BNT–0.05BNN ceramic. Through the formula: $\sigma = H/(RS)$, the conductivity of grain and grain boundary can be calculated, where H represents the thickness of the ceramic, R represents the grain resistance or grain boundary resistance, and S represents the surface area of electrode. And then, the activation energies of ~0.61 and 0.68 eV of the grains (Ea_g) and the grain boundaries (Ea_{gb}) are worked out by the Arrhenius-type curves, respectively. The magnitude of activation energy denotes that the conductive species of grains and grain boundaries in the ceramic samples are ascribed to the double ionized oxygen vacancies [47,48]. The formation of doubly ionized oxygen vacancies can be expressed by Kröger-Vink notation, as given below:

$$V_O^{\bullet\bullet} + \frac{1}{2}O_2 \rightarrow O_0^x + 2h^{\bullet} \quad (1)$$

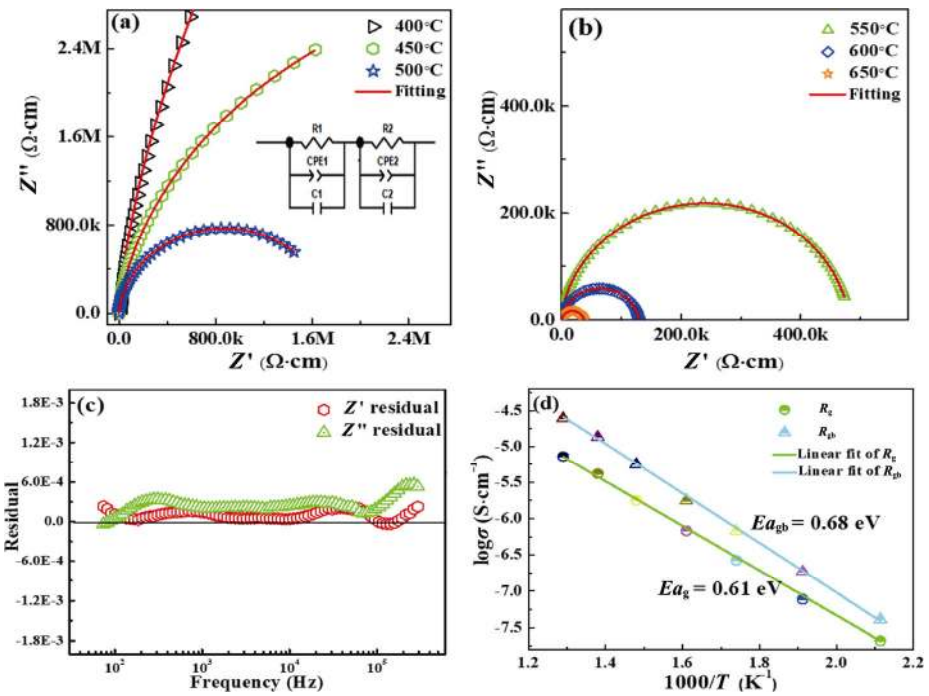

Fig. 6 Cole–Cole plots of 0.95BNT–0.05BNN ceramic samples were measured at temperatures of (a) 400–500 ℃ and (b) 550–650 ℃. The inset in (a) illustrates the fitting circuit model; (c) illustrates the impedance residuals of Z' and Z''; (d) illustrates the Arrhenius-type plots of 0.95BNT–0.05BNN ceramic under air atmosphere.

The optical properties of the ceramic samples are observed via the UV–Vis–NIR spectra. The light absorption of the all samples is shown in Fig. 7(a). Compared to pure $Bi_{0.5}Na_{0.5}TiO_3$ ceramic, the $BaNi_{0.5}Nb_{0.5}O_3$-doped $Bi_{0.5}Na_{0.5}TiO_3$ ceramics show broad light absorption spectrometer covering the range from visible light down to near-infrared (NIR) ($\lambda <$ 1600 nm). Meanwhile, the light absorption efficiency of the ceramics improves as the doping content increases. This material exhibits more potential advantages in the photovoltaic field. In Fig. 7(b), the optical bandgaps (E_g) of $BaNi_{0.5}Nb_{0.5}O_3$-doped $Bi_{0.5}Na_{0.5}TiO_3$ ceramics are determined by $(\alpha hv)^2 = A(hv–E_g)$, showing that the samples have three gap states corresponding to the absorption spectrum in Fig. 7(a) [40]. In the UV–Vis part, the band gaps decrease from 3.1 to 2.27 eV, which is lower than that of the typical BNT–SF ceramics (2.4 eV for 9 mol% Sr/Fe-added) [49]. The reduction in the optical bandgap may be related to the introduction of Ni ions. There is an obvious midgap state corresponding to Ni 3d between valence band maximum (VBM) of Ti 3d and conductive band minimum (CBM) of O 2p. Doping transition metals in $Bi_{0.5}Na_{0.5}TiO_3$ materials is predicted to generate a localized state between the bottom of conductive band and the top of valence band to reduce the optical bandgap, and the bandgap tuning mechanism with introduction of Ni ions is shown in the inset of Fig. 7(b) [50]. Therefore, the light absorption range of the samples can significantly broaden and the band gap can be reduced by the proper doping.

In this system, the 0.95BNT–0.05BNN ceramic has relatively high residual polarization strength, low band gap, and the largest J_{sc}. So, this component was selected for systematic study. The photocurrent density–voltage (J–V) curves measured both in the dark and under light illumination for 0.95BNT–0.05BNN ceramic are presented in Fig. 8(a). In the dark, the sample show near-zero dark current, while its photocurrent is clearly enhanced under light irradiation, a small open-circuit voltage (V_{oc}) of ~15.7 V and a short-circuit current density (J_{sc}) of ~1450 nA/cm^2 are obtained. Under the same measurement conditions, the J_{sc} and V_{oc} of x = 0.00, 0.10, 0.15, 0.20 compositions are 20.00, 1220, 1060, 930 nA/cm^2 and 2.0, 13.1, 11.5, 8.4 V, respectively. The photocurrent density for various compositions is presented in Table 1. The improvement of photocurrent in illumination can be attributed to the photo-generated carriers. The structural mechanism diagram of the ITO/BNNT/Ag device is shown in Fig. 8(e, upper). The 0.95BNT–0.05BNN ceramic is poled under the different poling field for 10 min in Fig. 8(b). The photocurrent gradually increases with the increase of poling field from 30 to 60 kV/cm. The sample was exposed to a polarized electric field of 60 kV/cm for 10 min; the greatly improved J_{sc} of ~5500 nA/cm^2 is obtained, which is 4 times higher than that of unpoled sample. To further analyze the effect of light intensity on photocurrent density, the light intensity-dependence of the output current is shown in Fig. 8(c). It can be observed from Fig. 8(c) that the output photocurrent gradually increases with the increase of light intensity from 50 to 200 mW/cm^2. This indicates that the light intensity can affect the activity of photogenerated carriers and further promote their separation, thus increasing the output current. It is reported that photocurrent density depends on many factors including bandgap, carrier mobility, wavelength, and intensity of light [51]. For ferroelectric semiconductors, the photocurrent is due to the following factors, including

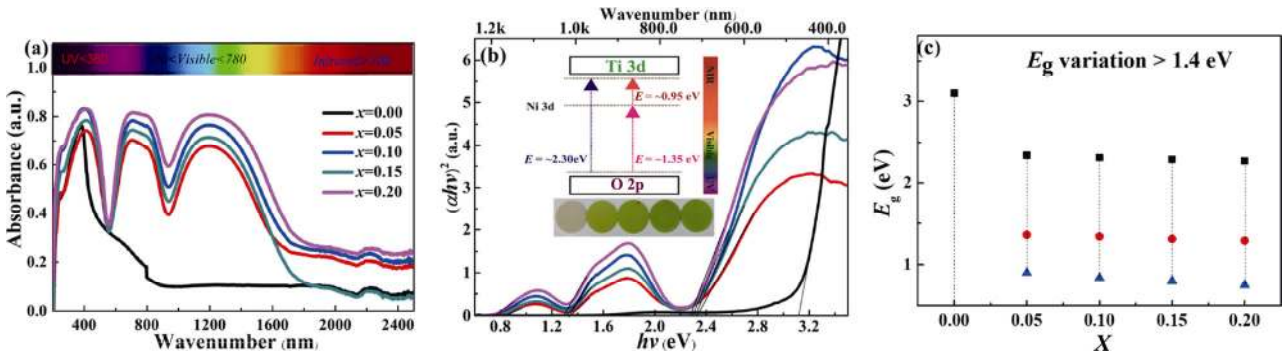

Fig. 7 (a) Absorbance spectra of pure and BNN-modified BNT materials. The inserted color bar was used to show the absorption at UV, visible, and NIR range; (b) band gap of (1–x)BNT–xBNN (x = 0.00–0.20) ceramic samples. The inset in (b) illustrates the bandgap tuning mechanism of the samples; (c) three sub-bandgap values of (1–x)BNT–xBNN (x = 0.00–0.20) ceramic samples are shown and dotted line shows the variation between the gap states of the samples.

Table 1 Photocurrent density of (1–*x*)BNT–*x*BNN (*x* = 0.00–0.20) ceramics

Composition	J_{sc} (nA/cm^2)	V_{oc} (V)	Composition	J_{sc} (nA/cm^2)	V_{oc} (V)
x = 0.00	20	2.0	x = 0.15	1060	11.5
x = 0.05	1450	15.7	x = 0.20	930	8.4
x = 0.10	1220	13.1			

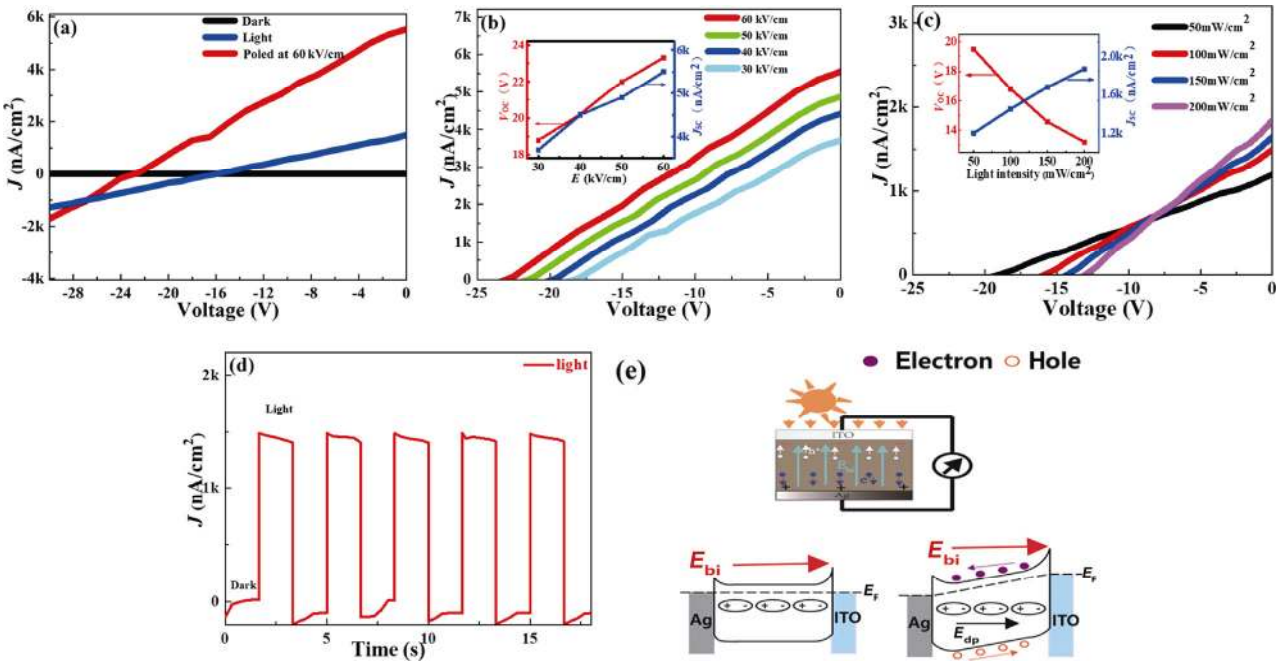

Fig. 8 (a) *J*–*V* curves under simulated AM1.5 sunlight of 100 mW/cm^2 for the 0.95BNT–0.05BNN sample; (b) *J*–*V* curves under different poling field for the 0.95BNT–0.05BNN ceramic at room temperature. The inset illustrates the open circuit voltage V_{oc} and short circuit current J_{sc} under different poling field; (c) *J*–*V* curves under different optical power densities of 0.95BNT–0.05BNN sample. The inset illustrates the open circuit voltage V_{oc} and short circuit current J_{sc} with different optical power densities; (d) photocurrent switching plots with the time of 0.95BNT–0.05BNN ceramic at room temperature; (e) structural mechanism diagram of the ITO/BNNT/Ag device is shown in the upper, and the electronic band diagram of the sample device in the polarization state is shown in the bottom.

the large residual polarization combined with a narrow band gap (E_g) and the Schottky barrier at the electrode interface of the ceramic samples [52]. It is easy to form Schottky barrier built-in field (E_{bi}) on unpolarized ITO/0.95BNT–0.05BNN/Ag devices. The net built-in electric field (E_{bi}) in the ITO/0.95BNT–0.05BNN/Ag device is from Ag to ITO because the Schottky barrier of ITO/0.95BNT–0.05BNN interface is much higher than that of Ag/0.95BNT–0.05BNN interface, as shown in Figs. 8(a)–8(e). The E_{bi} provides the driving force for photogenerated electron–hole pair separation in the bulk ceramic and induces the interface photovoltaic effects in unpoled 0.95BNT–0.05BNN ceramic. After positive poling, the depolarization electric field (E_{dp}) existing in the entire ferroelectrics has the same direction as the E_{bi}, which is beneficial for the separation of photogenerated electron–hole pairs, as shown in Figs. 8(b)–8(e). Therefore, a higher J_{sc} is obtained in the poled 0.95BNT–0.05BNN ceramic. The photocurrent and dark-current density conversion of 0.95BNT–0.05BNN ceramic is illustrated in Fig. 8(d). The observed photocurrent exhibits a fast and repeatable photo-response effect, just in line with the on/off photo-period. The results show that the BNT–BNN system is a promising candidate in the field of photovoltaics and photosensitive devices [53].

4 Conclusions

The (1–*x*)BNT–*x*BNN materials with x = 0.00–0.20 were successfully fabricated using the solid-state technique. This article systematically studies the crystal structures, photovoltaic properties, and electrical

characteristics of the system. The main phase of structure in the samples shows a perovskite crystalline structure. The ferroelectric properties of all samples at room temperature are verified by ferroelectric hysteresis. T_C ranges from 330 to 120 ℃ with increasing x. The BNT–BNN ceramics show low tanδ ($\leqslant$ 0.1) in the wide temperature range of 100–300 ℃. Observing from Cole–Cole plots, the sample had NTCR properties. The absorbance in the visible region has been significantly improved, and the band gap has been reduced from 3.1 to 2.27 eV. Under simulated sunlight illumination (AM1.5G, 100 mW/cm^2), a large J_{sc} of 1450 nA/cm^2 and a small V_{oc} of ~15.7 V can be obtained. A larger V_{oc} of 23 V and a higher J_{sc} of 5500 nA/cm^2 are achieved at the poling field of 60 kV/cm under the same light conditions. Superior optical properties make BNT–BNN ceramics an ideal candidate for photovoltaic applications. Our results have application potential in the field of ferroelectric photovoltaic.

Acknowledgements

This work was financially supported by the National Natural Science Foundation of China (Grant No. 11464006) and Guangxi Key Laboratory of Information Materials (Grant No. 191026–Z).

References

[1] Nayak PK, Mahesh S, Snaith HJ, *et al*. Photovoltaic solar cell technologies: Analyzing the state of the art. *Nat Rev Mater* 2019, **4**: 269–285.

[2] Zhang KW, Wang SH, Yang Y. A one-structure-based piezo-tribo-pyro-photoelectric effects coupled nanogenerator for simultaneously scavenging mechanical, thermal, and solar energies. *Adv Energy Mater* 2017, **7**: 1601852.

[3] Ma N, Zhang KW, Yang Y. Photovoltaic–pyroelectric coupled effect induced electricity for self-powered photodetector system. *Adv Mater* 2017, **29**: 1703694.

[4] Ji Y, Zhang KW, Yang Y. A one-structure-based multieffects coupled nanogenerator for simultaneously scavenging thermal, solar, and mechanical energies. *Adv Sci* 2018, **5**: 1700622.

[5] Chen L, Luo BC, Chan NY, *et al*. Enhancement of photovoltaic properties with Nb modified (Bi, Na) TiO_3–$BaTiO_3$ ferroelectric ceramics. *J Alloys Compd* 2014, **587**: 339–343.

[6] Chen J, Pei W, Chen G, *et al*. Greatly enhanced photocurrent in inorganic perovskite $[KNbO_3]_{0.9}[BaNi_{0.5}Nb_{0.5}O_{3-\sigma}]_{0.1}$ ferroelectric thin-film solar cell. *J Am Ceram Soc* 2018, **101**: 4892–4898.

[7] Qi J, Ma N, Yang Y. Photovoltaic-pyroelectric coupled effect based nanogenerators for self-powered photodetector system. *Adv Mater Interfaces* 2018, **5**: 1701189.

[8] Song K, Zhao RD, Wang ZL, *et al*. Sensors: Conjuncted pyro-piezoelectric effect for self-powered simultaneous temperature and pressure sensing. *Adv Mater* 2019, **31**: 1970257.

[9] Song K, Ma N, Mishra YK, *et al*. Achieving light-induced ultrahigh pyroelectric charge density toward self-powered UV light detection. *Adv Electron Mater* 2019, **5**: 1800413.

[10] Choi T, Lee S, Choi YJ, *et al*. Switchable ferroelectric diode and photovoltaic effect in $BiFeO_3$. *Science* 2009, **324**: 63–66.

[11] Qi J, Ma N, Ma XC, *et al*. Enhanced photocurrent in $BiFeO_3$ materials by coupling temperature and thermo-phototronic effects for self-powered ultraviolet photodetector system. *ACS Appl Mater Interfaces* 2018, **10**: 13712–13719.

[12] Zenkevich A, Matveyev Y, Maksimova K, *et al*. Giant bulk photovoltaic effect in thin ferroelectric $BaTiO_3$ films. *Phys Rev B* 2014, **90**: 161409.

[13] Ma N, Yang Y. Enhanced self-powered UV photoresponse of ferroelectric $BaTiO_3$ materials by pyroelectric effect. *Nano Energy* 2017, **40**: 352–359.

[14] Zhao K, Ouyang B, Yang Y. Enhancing photocurrent of radially polarized ferroelectric $BaTiO_3$ materials by ferro-pyro-phototronic effect. *iScience* 2018, **3**: 208–216.

[15] Ma N, Yang Y. Boosted photocurrent in ferroelectric $BaTiO_3$ materials via two dimensional planar-structured contact configurations. *Nano Energy* 2018, **50**: 417–424.

[16] Li DX, Shen ZY, Li ZP, *et al*. *P–E* hysteresis loop going slim in $Ba_{0.3}Sr_{0.7}TiO_3$-modified $Bi_{0.5}Na_{0.5}TiO_3$ ceramics for energy storage applications. *J Adv Ceram* 2020, **9**: 183–192.

[17] Zhang DL, Feng L, Huang WC, *et al*. Oxygen vacancy-induced ferromagnetism in $Bi_4NdTi_3FeO_{15}$ multiferroic ceramics. *J Appl Phys* 2016, **120**: 154105.

[18] Roukos R, Zaiter N, Chaumont D. Relaxor behaviour and phase transition of perovskite ferroelectrics-type complex oxides $(1–x)Na_{0.5}Bi_{0.5}TiO_3$–$xCaTiO_3$ system. *J Adv Ceram* 2018, **7**: 124–142.

[19] Li P, Li W, Liu S, *et al*. Reduced leakage current, enhanced ferroelectric and dielectric properties of (La, Fe)-codoped $Bi_{0.5}Na_{0.5}TiO_3$-based thin films. *Ceram Int* 2015, **41**: S344–S348.

[20] Li W, Zeng H, Hao J, *et al*. Enhanced dielectric and piezoelectric properties of Mn doped $(Bi_{0.5}Na_{0.5})TiO_3$–$(Bi_{0.5}K_{0.5})TiO_3$–$SrTiO_3$ thin films. *J Alloys Compd* 2013, **580**: 157–161.

[21] Gao Z, Zhang H, Liu Y, *et al*. An investigation on the dynamics of domain switching of $Bi_{0.5}Na_{0.5}TiO_3$-based ferroelectric ceramics. *Curr Appl Phys* 2017, **17**: 495–500.

[22] Acharya SK, Kim TM, Hyung JH, *et al*. Ferroelectric and

piezoelectric properties of lead-free $Bi_{0.5}Na_{0.5}TiO_3$–$Bi_{0.5}K_{0.5}TiO_3$–$BaTiO_3$-thin films near the morphotropic phase boundary. *J Alloys Compd* 2014, **586**: 549–554.

[23] Grinberg I, Vincent D, Torres M, *et al*. Perovskite oxides for visible-light-absorbing ferroelectric and photovoltaic materials. *Nature* 2013, **503**: 509–512.

[24] Xiao H, Dong W, Guo Y, *et al*. Design for highly piezoelectric and visible/near-infrared photoresponsive perovskite oxides. *Adv Mater* 2019, **31**: 1805802.

[25] Pang D, Liang T, Deng Y, *et al*. Dielectric, ferroelectric, and photovoltaic properties of La-doped $Bi(Ni_{2/3}Ta_{1/3})O_3$–$PbTiO_3$ ceramics. *J Alloys Compd* 2020, **815**: 152191.

[26] Han F, Zhang YJ, Yuan CL, *et al*. Photocurrent and dielectric/ferroelectric properties of $KNbO_3$–$BaFeO_{3-\delta}$ ferroelectric semiconductors. *Ceram Int* 2020, **46**: 14567–14572.

[27] Hue MM, Dung NQ, Trung NN, *et al*. Tunable magnetic properties of $Bi_{0.5}Na_{0.5}TiO_3$ materials via solid solution of $NiTiO_3$. *Appl Phys A* 2018, **124**: 1–7.

[28] Hung NT, Bac LH, Hoang NT, *et al*. Structural, optical, and magnetic properties of $SrFeO_{3-\delta}$-modified $Bi_{0.5}Na_{0.5}TiO_3$ materials. *Phys B*: *Condens Matter* 2018, **531**: 75–78.

[29] Dung DD, Hung NT, Odkhuu D. Structure, optical and magnetic properties of new $Bi_{0.5}Na_{0.5}TiO_3$−$SrMnO_{3-\delta}$ solid solution materials. *Sci Rep* 2019, **9**: 1–10.

[30] Dung DD, Hung NT. Structural, optical, and magnetic properties of the new $(1–x)Bi_{0.5}Na_{0.5}TiO_3 + xMgCoO_{3-\delta}$ solid solution system. *J Supercond Nov Magn* 2020, **33**: 1249–1256.

[31] Parija B, Badapanda T, Panigrahi S. Morphotropic phase boundary in BNT–BZT solid solution: A study by Raman spectroscopy and electromechanical parameters. *J Ceram Process Res* 2015, **16**: 565–571.

[32] Hue MM, Dung NQ, Phuong LTK, *et al*. Magnetic properties of $(1–x)Bi_{0.5}Na_{0.5}TiO_3 + xMnTiO_3$ materials. *J Magn Magn Mater* 2019, **471**: 164–168.

[33] Huang YM, Shi DP, Liu LJ, *et al*. High-temperature impedance spectroscopy of $BaFe_{0.5}Nb_{0.5}O_3$ ceramics doped with $Bi_{0.5}Na_{0.5}TiO_3$. *Appl Phys A* 2014, **114**: 891–896.

[34] Chen L, Luo BC, Chan NY, *et al*. Enhancement of photovoltaic properties with Nb modified (Bi, Na)TiO_3–$BaTiO_3$ ferroelectric ceramics. *J Alloys Compd* 2014, **587**: 339–343.

[35] Huang T, Hu ZG, Xu GS, *et al*. Inherent optical behavior and structural variation in $Na_{0.5}Bi_{0.5}TiO_3$–6%$BaTiO_3$ revealed by temperature dependent Raman scattering and ultraviolet-visible transmittance. *Appl Phys Lett* 2014, **104**: 111908.

[36] Hajra S, Pradhani N, Choudhary R, *et al*. Fabrication, dielectric and electrical characteristics of $0.94(BI_{0.5}Na_{0.5})TiO_3$–$0.06BaTiO_3$ ceramics. *Process Appl Ceram* 2019, **13**: 24–31.

[37] Kreisel J, Glazer AM, Bouvier P, *et al*. High-pressure Raman study of a relaxor ferroelectric: The $Na_{0.5}Bi_{0.5}TiO_3$ perovskite. *Phys Rev B* 2001, **63**: 174106.

[38] Niranjan MK, Karthik T, Asthana S, et al. Theoretical and experimental investigation of Raman modes, ferroelectric and dielectric properties of relaxor $Na_{0.5}Bi_{0.5}TiO_3$. *J Appl Phys* 2013, **113**: 194106.

[39] Kreisel J, Glazer AM, Jones G, *et al*. An X-ray diffraction and Raman spectroscopy investigation of A-site substituted perovskite compounds: The $(Na_{1-x}K_x)_{0.5}Bi_{0.5}TiO_3$ ($0 \leqslant x \leqslant 1$) solid solution. *J Phys*: *Condens Matter* 2000, **12**: 3267–3280.

[40] Chen ZX, Yuan CL, Liu X, *et al*. Optical and electrical properties of ferroelectric $Bi_{0.5}Na_{0.5}TiO_3$–$NiTiO_3$ semiconductor ceramics. *Mater Sci Semicond Process* 2020, **115**: 105089.

[41] Han F, Zhang YJ, Yuan CL, *et al*. Impedance spectroscopy and photovoltaic effect of oxygen defect engineering on $KNbO_3$ ferroelectric semiconductors. *J Electron Mater* 2020, **49**: 6165–6174.

[42] Bai W, Chen D, Huang Y, *et al*. Temperature-insensitive large strain response with a low hysteresis behavior in BNT-based ceramics. *Ceram Int* 2016, **42**: 7669–7680.

[43] Kim JS, Choi BC, Jeong JH, *et al*. Low-frequency dielectric dispersion and impedance spectroscopy of lead-free $(Na_{0.5}Bi_{0.5})TiO_3$(NBT) ferroelectric ceramics. *J Korean Phy Soc* 2009, **55**: 879–883.

[44] Zeb A, Hall DA, Milne SJ. Lead-free piezoelectric $K_{0.5}Bi_{0.5}TiO_3$–$Bi(Mg_{0.5}Ti_{0.5})O_3$ ceramics with depolarisation temperatures up to ~220 ℃. *J Mater Sci*: *Mater Electron* 2015, **26**: 9516–9521.

[45] Zeb A, Bai Y, Button T, *et al*. Temperature-stable relative permittivity from −70 ℃ to 500 ℃ in $(Ba_{0.8}Ca_{0.2})TiO_3$–$Bi(Mg_{0.5}Ti_{0.5})O_3$–$NaNbO_3$ ceramics. *J Am Ceram Soc* 2014, **97**: 2479–2483.

[46] Hajra S, Sahoo S, Das R, et al. Structural, dielectric and impedance characteristics of $(Bi_{0.5}Na_{0.5})TiO_3$–$BaTiO_3$ electronic system. *J Alloys Compd* 2018, **750**: 507–514.

[47] Yan X, Chen X, Li X, *et al*. Good electrical performances and impedance analysis of $(1–x)$KNN–xBMM lead-free ceramics. *J Mater Sci*: *Mater El* 2018, **29**: 4538–4546.

[48] Liu L, Huang Y, Su C, *et al*. Space-charge relaxation and electrical conduction in $K_{0.5}Na_{0.5}NbO_3$ at high temperatures. *Appl Phys A* 2011, **104**: 1047–1051.

[49] Hung NT, Bac LH, Hoang NT, *et al*. Structural, optical, and magnetic properties of $SrFeO_{3-\delta}$-modified $Bi_{0.5}Na_{0.5}TiO_3$ materials. *Phys B*: *Condens Matter* 2018, **531**: 75–78.

[50] Dung DD, Thiet DV, Odkhuu D, *et al*. Room-temperature ferromagnetism in Fe-doped wide band gap ferroelectric $Bi_{0.5}K_{0.5}TiO_3$ nanocrystals. *Mater Lett* 2015, **156**: 129–133.

[51] Cao L, Ding Z, Liu X, *et al*. Photovoltaic properties of Aurivillius $Bi_4NdTi_3FeO_{15}$ ceramics with different orientations. *J Alloys Compd* 2019, **800**: 134–139.

[52] Wu L, Podpirka A, Spanier JE, *et al*. Ferroelectric, optical,

and photovoltaic properties of morphotropic phase boundary compositions in the $PbTiO_3$–$BiFeO_3$–$Bi(Ni_{1/2}Ti_{1/2})O_3$ system. *Chem Mater* 2019, **31**: 4184–4194.

[53] Han F, Zhang YJ, Yuan CL, *et al*. Photocurrent and dielectric/ferroelectric properties of $KNbO_3$–$BaFeO_{3-\delta}$ ferroelectric semiconductors. *Ceram Int* 2020, **46**: 14567–14572.